# Development, Control, and MRI-Compatibility of the MR-SoftWrist

Andrew Erwin*, Marcia K. O'Malley*, David Ress†, and Fabrizio Sergi*‡

***Abstract*— This paper presents the MR-SoftWrist: a parallel 3DOF MR-compatible wrist robot with compliant actuation. Through a design that aligns the wrist joint axes to the device DOFs and uses custom MR-compatible force-feedback actuation, the MR-SoftWrist can measure and support wrist movements during fMRI. The device has a circular workspace for wrist flexion/extension and radial/ulnar deviation with 18 deg radius, and is capable of generating 1.75 Nm joint torque. Control experiments validate the device's workspace, along with position and zero torque control capabilities. In zero torque mode the maximum force felt by the user is 0.15 Nm, less than 10% of the device's torque output. The device is shown to have no significant affect on imaging quality during fMRI.**

## I. Introduction

Rehabilitation robots have demonstrated their effectiveness in improving functional outcomes of patients with neurological disorders; however, the underlying mechanisms that promote recovery from a neurological injury are still not well understood [1]. As a result, optimal therapeutic regimens remain to be found in neurorehabilitation [2]. One approach to understanding the recovery process at the neurological level is the use of functional magnetic resonance imaging (fMRI) in conjunction with a haptic interface. With the aid of a robot that can display arbitrary dynamics to the user, rehabilitation-like protocols can be performed during fMRI to determine which best promote recovery [3]. Using a haptic interface is necessary in this endeavor for its force control, backdrivability, repeatability, accuracy, and precision [4].

To be used during fMRI, the haptic device must be MR-compatible, and in particular the robot must not pose any hazards to the user, have any degradation in performance from the scanner, and not affect quality of scanned images [4]. Thus far, researchers have developed two strategies to address the constraints imposed by the MR environment [5]. The first is a remote actuation scheme where non-compatible actuators and materials are located at a great distance ($>$1 m) from the user and are connected to the end effector through hoses (when using fluidic actuation) or long rods (when using electromechanical actuation) [6], [7]. The alternative solution is to co-locate the actuators with the end effector, requiring all materials and actuators to be MR-compatible [8].

Several remotely actuated single- and multi-DOF designs have been proposed in the literature. Two prominent approaches were the use of pneumatics to perturb hand movements [9], and a hydraulic solution to control either wrist-elbow or elbow-shoulder movements [10]. While these solutions offer suitable range of motion (ROM) and producible force, they have limited position and force control bandwidth. An alternative remote solution was to use long rods connected to a Phantom Premium [7]. Improving on this solution, Menon et al. developed a version using MR-compatible materials, while locating the DC motors in a Faraday Cage [11]. The two previous remotely actuated 3DOF devices used long carbon fiber rods to interact with the user's hand in an end effector design which has potential degradation of force bandwidth and accuracy.

Co-located actuation approaches have been developed for 1DOF systems [8], and designs have been proposed for multi-DOF systems [12]. In [12], a parallel 6-R structure was proposed which uses six ultrasonic motors (USMs) to interact with the user for pick-and-place tasks involving the hand, wrist, and elbow. Each of the previous devices require custom MR-compatible force sensors and have not demonstrated interaction control capabilities.

This paper presents the MR-SoftWrist, a parallel 3DOF co-located haptic MR-compatible robot for wrist motor protocols during fMRI (Fig. 1). The device architecture, first introduced by our group in [13], employs series elastic actuation (SEA) to achieve interaction control. By aligning the user's wrist axes with those of the robot, measurement and support of wrist flexion/extension (FE) and radial/ulnar deviation (RUD) is achieved. To our knowledge, this paper is the first to demonstrate an MR-compatible multi-DOF wrist robot with co-located actuation with capabilities for both position and interaction control.

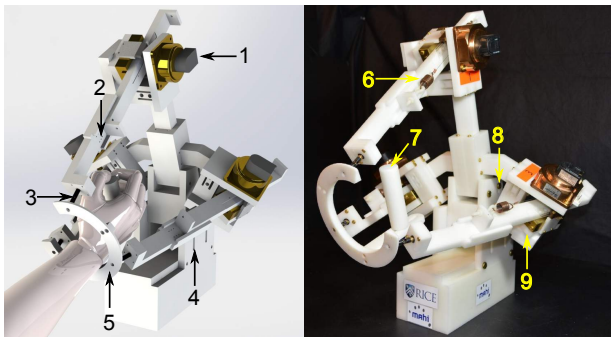


Fig. 1. (left) CAD image of the MR-SoftWrist and (right) fabricated device. 1) Ultrasonic motor, 2) platform height adjustment holes, 3) universal joint, 4) vertical height adjustment slot, 5) wrist ring, 6) extension spring, 7) handle, 8) angular adjustment slot, and 9) revolute-prismatic joint.

This work was supported in part by a TIRR Memorial Hermann Pilot grant, by the NSF GRFP under Grant No. 0940902, and by the NSF CNS-1135916. *: Mechatronics and Haptic Interfaces Laboratory, Department of Mechanical Engineering, Rice University, Houston, TX 77005. †: Department of Neuroscience, Baylor College of Medicine, Houston, TX 77030. ‡: Biomedical Engineering, University of Delaware, Newark, Delaware 19716. Corresponding author: fabs@rice.edu.

## II. MR-Compatible Wrist Robot

By combining measurements of brain activity during wrist sensorimotor tasks with therapeutic protocols delivered through a rehabilitation robot, we can examine the task-specific modulation of brain activity via robot-assisted training. By targeting wrist movements instead of more proximal limbs as done in [9]–[11], we expect to obtain reduced head movements and moving body mass during scanning, thus improving fMRI image quality [14]. To achieve therapy-like protocols during fMRI, the device needs to have accurate position, low-impedance, and force-source control modes [15], [16], with a circular workspace of radius 20 deg for wrist FE and RUD, and 1.5 Nm of continuous torque [13].

### A. Device Structure and Actuation

*1) Kinematic Structure:* A parallel design was pursued for its increased structural rigidity and torque output as compared to a serial design. Additionally, the parallel design places the actuators on a stationary base frame, reducing potential imaging artifacts from active electrical components moving in the scanner's magnetic field. A 3RPS kinematic structure (see Fig. 2) was chosen which consists of a base ring and three legs, each of which include a revolute, prismatic (actuated), and spherical joint [17]. Each spherical joint is mounted equidistantly on a wrist ring, which is the robot end-effector with 3DOFs corresponding to $z_c$ (the platform height), $\alpha$ (wrist FE, a positive rotation about $\hat{x}$), and $\beta$ (RUD, a positive rotation about $\hat{y}$). Although $z_c$ is a DOF of the device, it is fixed during operation so that the user's wrist axes remain aligned with the device's axes. The nominal configuration of the device is when $\alpha = \beta = 0$ and $z_c = z_{c,nom}$ which corresponds to the extensible links $l_i$ being equal to $l_{i,nom}$.

A design was pursued such that the user's hand moves in the space between the base and wrist rings (see Fig. 1(a)). This solution places the actuators far from the scanner bore, which is beneficial for the device's performance and for avoiding interference with scanned images. Additionally, fixing the forearm during operation allows for measurement and support of wrist FE and RUD. A drawback of this solution is that it requires large values for the wrist ring radius ($r$) and base ring radius ($R$) to fit the user's hand inside the device, since if $r$ isn't large enough, the extensible links ($l_i$) will make contact with the user's hand.

A relevant measure of the robot workspace size is the radius of the circle inscribed within admissible solutions in the 2D task space defined by the selection of a specific $z_{c,nom}$ value. Such a measure is largely determined by $r$, and it increases as $\frac{1}{r}$. The distance between the two rings ($z_{c,nom}$) must be large enough for the hand to fit between them. As the distance is increased, the actuators can be placed further from the scanner isocenter; however, this increase comes at the cost of reduced workspace size and structural stiffness. Thus, parameters $r$, $R$, and $z_{c,nom}$ were carefully selected to guarantee a large workspace size while avoiding interference between the subject's hand and the moving links, as well as between the device and the scanner bore. The effect of $r$, $R$ and $z_{c,nom}$ on the workspace radius can be seen in Fig. 3.

*2) Structural Parameter Selection and Adjustability:* Values for $z_{c,nom}$, $R$, and $r$ were chosen that could meet the target 20 deg circular ROM, while also fitting the user's hand inside the device. The values chosen were 240 mm for $z_{c,nom}$ (corresponding to 263 mm for $l_{i,nom}$), 168 mm for $R$ and 66 mm for $r$. CAD renderings showed that for the given set of $z_{c,nom}$, $R$, and $r$ the user's hand would make contact with the device in just over the target 20 deg workspace which corresponded to 41 mm of total link travel. Due to a limited selection in MR-compatible linear bearings, the chosen bearings with the closest travel had 39 mm of travel, thus decreasing the reachable workspace to 19 degrees.

To accommodate different users, adjustability was built into the device in several ways as shown in Fig. 1. The device structure consists of a large base to ground the device and a vertical and angular adjustment for aligning the user's

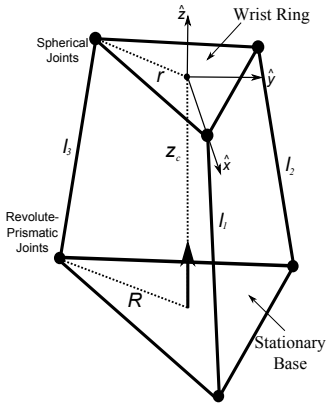


Fig. 2. Kinematic schematic of the MR-SoftWrist with relevant parameters labeled. A stationary base with radius $R$ is connected to a moving platform with radius $r$ through extensible links with length $l_i$, corresponding to a platform height $z_c$. This figure is adapted from [16], [17].

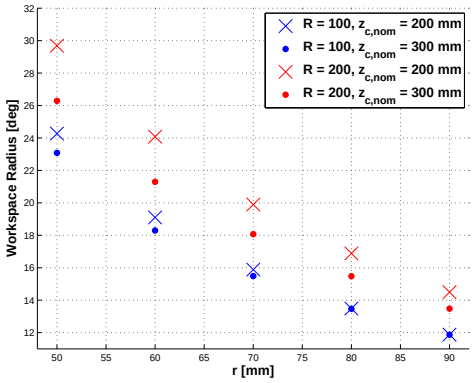


Fig. 3. Variation in workspace radius (of a circle for $\alpha$ and $\beta$) dependent on $r$, $R$, and $z_{c,nom}$. To maximize this radius, $r$ was minimized while ensuring that the user's hand would not contact the links while inside the workspace, $R$ was maximized before the device would contact the scanner, and $z_{c,nom}$ was chosen to place the device just at the edge of the scanner.

wrist with the axes of the wrist ring. The parameters $R$ and $z_{c,nom}$ were made adjustable with three different values each, making nine different device configurations possible and so requiring nine possible values for $l_{i,nom}$. For the nine possible combinations, the device can achieve 19±1 degrees of workspace. Table I summarizes the values of the parameters presented in this section.

TABLE I
MR-SOFTWRIST STRUCTURAL PARAMETERS

| $z_{c,nom}$ [mm] | $R$ [mm] | $r$ [mm] | Workspace Radius [deg] |
|---|---|---|---|
| [210 240 268] | [155 168 180] | 66 | 19±1 |

*3) Components:* The MR-SoftWrist is a co-located robot, requiring all components to be MR-compatible. Structural components are made from Delrin, while brass is used for all structural screws. The actuated prismatic joints are linear SEAs composed of rotary USMs (Shinsei Corp. USR60-E3NT 60W), connected to custom brass extension springs (Spring Engineers of Houston LTD.) through a cable transmission (SpiderWire Stealth 0.4 mm diameter braided fishing line, 80 lb test). The springs are connected to a slider through nylon eyebolts which are also used for pre-tensioning the springs. Load deflection is measured through a linear optical encoder (US Digital EM1-0-500-I). The slider is supported by brass housed linear bearings with ceramic balls and titanium shafts (Del-Tron Precision Inc. S2-1.5-NMS-Brass), while the linear actuated modules are supported by ceramic radial bearings (Impact Bearing). The spherical joints are approximated by an RUR chain. The universal joint (Ondrives US Corp. size 6 plastic universal joint) is made of brass and Delrin while the two radial bearings (Boca Bearings) are ceramic. Using two radial bearings introduces redundancy, which does not affect kinematics [16], in the kinematic chain allowing for greater ROM since the universal joints are less restricted.

### B. Theoretical Characteristics of the MR-SoftWrist

Theoretical performance characteristics with respect to the device's operational 2DOF ($\alpha$ and $\beta$ since $z_c$ is fixed during operation) are obtained using the device's nominal structural parameters ($R = 168$ mm and $l_{i,nom} = 263$ mm). Although the results will change slightly depending on these structural values, the results below give a representative sample of how the device's performance changes as the link lengths are varied throughout the device's workspace, meaning $l_i$ are within the bearing limits. To obtain performance characteristics as the device configuration changes in the allowable workspace, the device Jacobian is required and is defined as

$$\dot{\mathbf{q}} = \mathbf{J}\dot{\mathbf{x}} \tag{1}$$

where $\dot{\mathbf{q}} = [\dot{l}_1 \ \dot{l}_2 \ \dot{l}_3]^T$ is a vector of joint space velocities, $\dot{\mathbf{x}} = [\dot{z}_c \ \dot{\alpha} \ \dot{\beta}]^T$ is a vector of task space velocities, and $\mathbf{J}$ is the device Jacobian which is a 3x3 matrix.

*1) Velocity and Torque Limits:* To determine the maximum possible velocities $\dot{\alpha}$ and $\dot{\beta}$ for every configuration in the workspace, the inverse Jacobian was used to relate the maximum joint space velocities to the task space ones as

$$\dot{\mathbf{x}} = |\mathbf{J}^{-1}\mathbf{k}\dot{q}_{max}| \ \forall \ \mathbf{q} \subset W \tag{2}$$

where $W$ is the workspace of the device, $\mathbf{k} = [k_1 \ k_2 \ k_3]^T$ is a vector of scalar values between ±1, and $\dot{q}_{max}$ is the maximum joint space velocity of 86 mm/s. The maximum task space velocities at each configuration are found through careful selection of the components of $\mathbf{k}$. Using (2) leads to a system of three equations which can be solved by satisfying constraints that 1DOF be maximized while the other DOF and $z_c$ have zero velocity. For example, for the configuration $\alpha = \beta = 0$, $\dot{\alpha}_{max}$ is obtained with $\mathbf{k} = [0 \ 1 \ -1]^T$ and $\dot{\beta}_{max}$ with $\mathbf{k} = [1 \ -0.5 \ -0.5]^T$. Using this method in (2) for all possible configurations, the resulting maximum angular velocities are $\dot{\alpha} =$ 1.43-2.05 rad/s and $\dot{\beta} =$ 1.24-2.04 rad/s.

The maximum torque for every possible configuration was found in a similar way, except that the equation relating joint space forces to task space torques is given by

$$\mathbf{f_E} = |\mathbf{J}^T\mathbf{k}f_{L,max}| \ \forall \ \mathbf{q} \subset W \tag{3}$$

where $f_{L,max}$ is the maximum linear task space force and $\mathbf{f_E} = [F_z \ \tau_\alpha \ \tau_\beta]^T$ are the task space forces and torques. The maximum load force is limited by the springs since their yield deflection occurs at 25 N. Note that this force on the USM only corresponds to 0.138 Nm, which is almost 4 times less than its maximum continuous torque of 0.5 Nm. The resulting maximum end-effector torques for $\alpha$ and $\beta$ are 1.86-2.83 Nm and 1.76-2.46 Nm respectively.

### C. Spatial and Torque Resolution

Spatial resolution of the device was computed as

$$\delta_x = \max\{|\mathbf{J}^{-1}\mathbf{k}\delta_q| \ \forall \ \mathbf{q} \subset W\} \tag{4}$$

where $\delta_q$ is the joint space position resolution and $\delta_x$ are the task space spatial resolutions. The joint space resolution is obtained from the resolution of the linear optical encoders, which have a resolution of 0.0127 mm of link travel using a quadrature reading. Applying this in (4) results in a maximum quantization of $3 \times 10^{-4}$ rad for $\alpha$ and $\beta$.

The torque resolution of the device is computed as

$$\delta_{f_E} = \max\{|\mathbf{J}^T\mathbf{k}\delta_{f_L}| \ \forall \ \mathbf{q} \subset W\} \tag{5}$$

where $\delta_{f_L}$ and $\delta_{f_E}$ are the joint and task space force resolutions respectively. The USM has a 1000 cnt/rev encoder corresponding to 0.0086 mm of link travel, and with a spring constant of 3.8 N/mm, summing the resolutions of the USM and load encoders leads to a worst case resolution of 0.08 N. Applying this in (5) leads to a maximum quantization of 9 mNm for $\alpha$ and $\beta$ which is 0.5% of the 1.75 Nm maximum interaction torque.

### D. Signal filtering and shielding

The MR-SoftWrist includes several electrically active components, i.e. six optical encoders and three USMs (voltages on the order of 200 V at 40-45 kHz). Operation of such elements during imaging can introduce electromagnetic interference (EMI), if the signal is not filtered properly to a ground reference, such as the one provided by the scanner penetration panel. In an effort to reduce EMI introduced by active device components, tripolar twisted-pair shielded cable with an additional outer shield was used for encoder lines, and the optical encoder cases were wrapped with aluminum foil. The USMs were wrapped in aluminum foil along with their respective encoders. Connection of the shield of the cable to the foil on one side and to the penetration panel on the other ensured a low-impedance path to ground, attenuating the noise generated by active components through a Faraday cage. To ensure decoupling of the signal references and to avoid introducing noise in the scanner room coming from the unshielded control room, the encoder lines and motor power lines were low-pass filtered using 5.6 pF and 1.3 pF capacitive filters respectively, with the frame of the filters connected to the penetration panel.

## III. Experimental Validation

### A. Control

Control of the MR-SoftWrist was performed through real-time software in a Matlab-Simulink model communicating with Quanser's Q8 USB board at a 1 KHz loop rate. Of most importance for control were the device Jacobian and the forward and inverse kinematics. The device Jacobian was obtained through the formulation found in [18]. In [18] the Jacobian is given as $\rho(q')$, where $\mathbf{q}'$ is a vector of all 12 generalized coordinates, which is a matrix relating task space to joint space velocities. We obtained a closed form of the inverse kinematics through a method similar to that presented in [17] while the forward kinematics required an iterative solution as discussed in [19].

To evaluate the ability of the load to track a sinusoidal profile, a circle in task space coordinates with frequency 0.3 Hz and radius 18 deg was specified as a reference. Control of the device was accomplished through a simple task space position control scheme as shown in Fig. 4. The task space controller converts an error into a desired USM velocity, which is regulated with the USM's factory tuned velocity controller [13]. The result of applying this control scheme to the circular task space reference can be seen in Fig. 5. This plot validates the workspace of the device as well as shows its capabilities in tracking sinusoidal positions accurately.

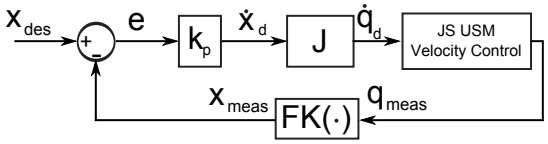


Fig. 4. Block diagram of the task space position controller for the MR-SoftWrist. Desired task space position ($\mathbf{x_{des}}$), measured task space position ($\mathbf{x_{meas}}$), error ($\mathbf{e}$), proportional gain ($\mathbf{k_p}$), desired task space velocity ($\dot{\mathbf{x}}_\mathbf{d}$), Jacobian ($\mathbf{J}$), desired joint space velocity ($\dot{\mathbf{q}}_\mathbf{d}$), USM velocity controller, measured joint space position ($\mathbf{q_{meas}}$), and forward kinematics (FK($\cdot$)).

Interaction control of the device was realized through the task space impedance control scheme shown in Fig. 6. To implement zero torque control, the virtual spring constant ($\mathbf{k_v}$) is the null vector resulting in the desired task space torques being equal to zero. The low-level zero force controller presented in [13] was implemented on each actuation module. Such a cascaded force-velocity SEA controller contains a proportional gain for the outer force loop which determines the control effort based on force measurement error. Here we present an experiment where the user attempts to perform wrist FE for various velocities. As can be seen in Fig. 7, the user essentially feels a damping force proportional to velocity as the user performs wrist FE. Note that the slope of this curve gives the effective damping coefficient which is inversely proportional to the proportional gain ($k_{p,i}$) used in the low-level zero force controller. From Fig. 7, with the user specifying a maximum expected velocity of 2 rad/s, the user only needs to provide 0.15 Nm of torque, corresponding to less than 10% of the maximum producible torque.

### B. MR-Compatibility

A set of experiments was performed to determine if the SEA MR-SoftWrist can function inside the MRI room as well as not distort images obtained during fMRI. The first requirement of MR-compatibility, namely safety due to ferrous components, was not of concern since the device is made entirely of low susceptibility components. MR-compatibility scans were conducted at the Baylor College of Medicine Center for Advanced MR Imaging, using a Siemens 3T MAGNETOM Trio with a 12 channel head coil and 60 cm bore.

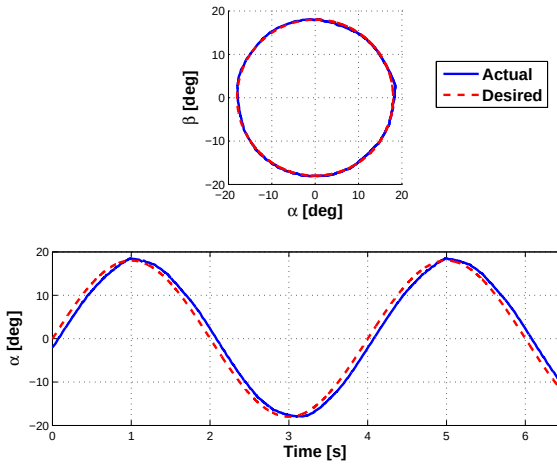


Fig. 5. Experimental position control results for tracking a 0.3 Hz 18 degree radius circular reference in task space coordinates. (Top) Tracking performance in task space coordinates validating the workspace of the device. (bottom) Shows the device's tracking capabilities with respect to time to illustrate that the device accurately tracks the reference trajectory.

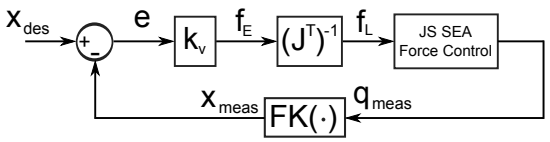


Fig. 6. Block diagram of task space impedance control specifying a virtual stiffness for the MR-SoftWrist. Virtual spring stiffness ($\mathbf{k_v}$), task space forces and torques ($\mathbf{f_E}$), joint space load forces ($\mathbf{f_L}$), and force control performed at the joint space level as in [13]. See Fig. 4 for other variables.

*1) Methods:* We assessed MR-compatibility of the MR-SoftWrist through two different experiments, one used to detect noise at specific frequencies (RF noise test), and the other to assess the introduction of higher temporal fluctuation in the fMRI signal, through measurement of the temporal noise-to-signal ratio (tNSR) during fMRI sequences. Each excitation protocol was conducted in three different experimental conditions, i.e. baseline (BL), device in (IN), device moving (MVT). In the BL condition, only the phantom was in the scanner. In the IN condition, the device was located at a position representative of its normal operation (see Fig. 9). In the MVT condition, the device was commanded to track 6 mm peak-to-peak sinusoidal joint space movements.

In the RF noise test, an excitation signal with a linearly increasing frequency (123.2±1.25 MHz, with a spacing of 196 Hz, for a total of 12800 excited frequencies) is applied to the coil, and the corresponding signal intensity is measured. In this test, the MR scanner coil is essentially used as an RF spectrometer to assess the presence of specific frequencies in which abnormal absorption of RF signal is detected. This test was repeated multiple times to troubleshoot the specific shielding and grounding conditions of active encoder lines, until no significant increase of signal intensity was observed at any frequency, when comparing the BL and the IN conditions.

tNSR, a measure proposed in [20] and introduced in the MR-compatible robotics literature in [21], involves scanning a phantom with electrical properties matching the ones of a human head. For this purpose, a spherical phantom filled with doped agar gel was used. A standard T2-weighted sequence employed in fMRI studies was used[1]. Processing of tNSR involved definition of a Region-Of-Interest (ROI), a rectangular set of 16x16x21 adjacent voxels in the center of the phantom, resulting in a total of 5376 voxels. Signal intensity measured from each voxel $i$ was concatenated in a timeseries $s_i$, with mean $\bar{s}_i$, that was detrended using a linear regression. Detrending increases specificity of the measurement, compensating for the slower thermal scanner dynamics in the computation of temporal fluctuations of the signal. From the detrended timeseries $\check{s}_i$, noise $n_i$ was calculated as

$$n_i = \text{median}(|\check{s}_i|), \tag{6}$$

[1]voxel size=2.5x2.5x2.5 mm, image size=80x80 px, flip angle=78, TE=35 ms, TR=2000 ms, no. slices=38

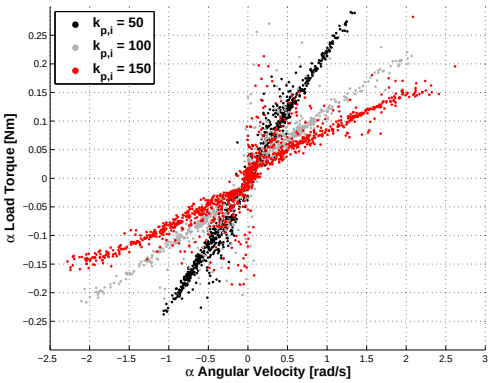


Fig. 7. Experimental validation of zero torque control for wrist FE with the joint space data filtered using a Savitzky-Golay filter and down-sampled for visualization to 50 Hz. The plot shows that as the proportional gain ($k_{p,i}$) at the joint space level is increased, the damping felt by the user is decreased. Note that the units of the gain $k_{p,i}$ are in $\text{ms}^{-1}\text{N}^{-1}$.

and tNSR was calculated as percentage of the mean time-series signal, as

$$\text{tNSR}_i = \frac{n_i}{\bar{s}_i} \times 100. \tag{7}$$

MR-compatibility was assessed through a non-parametric Kruskal-Wallis test, comparing the distributions of tNSR from all 5376 voxels, in the three experimental conditions BL, IN, and MVT. It is worth noting that this test is very conservative for the rejection of the null hypothesis, since it assumes that each of the 5376 measurement is independent, while instead there is strong spatial correlation of signal and noise intensities acquired from adjacent voxels. In fact, previous uses of tNSR (or of its reciprocal tSNR) in the robotics literature evaluated only a subset of voxels that can be considered for the analysis, including only 49 voxels [22] or a slice-wise comparison [21].

*2) Results:* No significant difference was determined for the effect of "experimental condition" on tNSR, as demon-

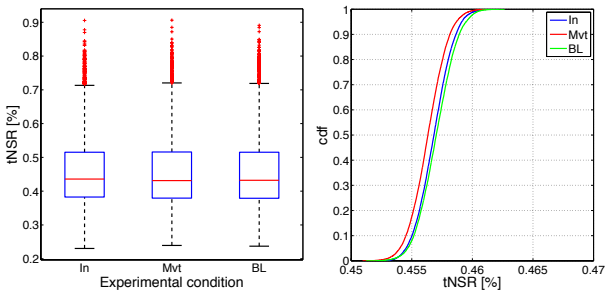


Fig. 8. (a) Box plot describing the distribution of tNSR in different experimental conditions (red line indicates the median, box edges indicate the 25th ($q_1$) and 75th ($q_3$) percentile, whiskers extend to $q_3 + 1.5(q_3 - q_1)$ and $q_1 - 1.5(q_3 - q_1)$; measurements outside this range are reported as outliers. (b) Cumulative distribution function estimated through bootstrapping of the tNSR distributions, which allows computation of non-parametric confidence intervals.

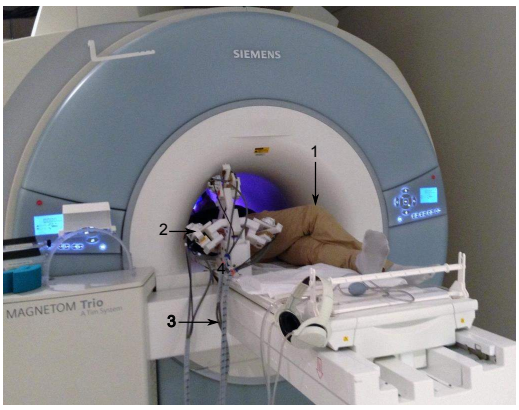


Fig. 9. MR-SoftWrist location during fMRI. 1) Subject, 2) MR-SoftWrist, and 3) encoder and power lines.

strated by the Kruskal-Wallis test ($p = 0.40$), (see Fig. 8(a)). This is also confirmed by estimate of the cumulative distributions of tNSR obtained through bootstrapping ($N = 10000$, Fig. 8(b)), which estimates the tNSR confidence intervals to be $0.457 \pm 0.003$ for the IN condition, $0.456 \pm 0.003$ for the MVT condition, and $0.457 \pm 0.003$ for the BL condition.

In addition to showing MR-compatibility with respect to not disturbing images, the effect of the scanner on the MR-SoftWrist was examined. Movement data of the device from the MVT condition was compared to the same protocol executed inside the control room. Comparing the data, the maximum position error of any link was 0.38 mm, a maximum full-scale-output error of 6%. This is a reasonable result since when comparing the two MVT conditions data, a similar maximum error of 0.34 mm and maximum full-scale-output error of 4% were found, indicating that the device did not lose any functional abilities due to the MR scanner.

## IV. Discussion and Conclusions

In this paper, the design and fabrication of a parallel 3DOF co-located haptic MR-compatible robot was presented. A parallel architecture was exploited for its increased structural rigidity, velocity, and torque output along with benefits for scanned image quality since the actuators are housed on a stationary base and are located far from the isocenter. Through careful selection of structural parameters, the device has a circular workspace of 18 deg radius for wrist FE and RUD and can be adjusted to accommodate different users. The device is capable of producing greater than 1.24 rad/s of angular velocity and 1.75 Nm of torque, along with spatial and force resolutions of $3 \times 10^{-4}$ rad and 9 mNm respectively for each joint. A position control experiment validated the workspace of the device and showed accurate tracking performance. Interaction control capabilities were evaluated through a zero torque experiment which showed that the maximum load torque felt by the user was less than 10% of the maximum 1.75 Nm load torque. Finally, MR-compatibility was assessed and showed that the device in operation during fMRI had no significant effect on image quality. This paper is the first to present an MR-compatible device for measuring and assisting wrist movements with demonstrated interaction control and MR-compatibility.

## References

[1] A. C. Lo *et al.*, "Robot-assisted therapy for long-term upper-limb impairment after stroke," *New England J. Med.*, vol. 362, no. 19, pp. 1772–1783, 2010.

[2] N. Hogan *et al.*, "Motions or muscles? Some behavioral factors underlying robotic assistance of motor recovery," *J. Rehab. Res. Dev.*, vol. 43, no. 5, p. 605, 2006.

[3] L. Marchal-Crespo *et al.*, "An fMRI pilot study to evaluate brain activation associated with locomotion adaptation," in *IEEE Int. Conf. Rehab. Robot. (ICORR)*, 2011, pp. 1–7.

[4] R. Gassert, E. Burdet, and K. Chinzei, "Opportunities and challenges in MR-compatible robotics," *IEEE Eng. Med. Biol. Mag.*, vol. 27, no. 3, pp. 15–22, 2008.

[5] F. Sergi *et al.*, "Compliant force-feedback actuation for accurate robot-mediated sensorimotor interaction protocols during fMRI," in *IEEE RAS & EMBS Int. Conf. Biomed. Robot. and Biomech. (BioRob)*, 2014, pp. 1057–1062.

[6] R. Gassert *et al.*, "Actuation methods for applications in MR environments," *Concepts Magn. Reson. Part B: Magn. Reson. Eng.*, vol. 29, no. 4, pp. 191–209, 2006.

[7] A. Hribar and M. Munih, "Development and testing of fMRI-compatible haptic interface," *Robotica*, vol. 28, no. 02, pp. 259–265, 2010.

[8] M. Flueckiger *et al.*, "fMRI compatible haptic interface actuated with traveling wave ultrasonic motor," in *IEEE Ind. Appl. Soc. (IAS)*, vol. 3, 2005, pp. 2075–2082.

[9] J. Diedrichsen *et al.*, "Neural correlates of reach errors," *J. Neuroscience*, vol. 25, no. 43, pp. 9919–9931, 2005.

[10] R. Gassert *et al.*, "A 2-DOF fMRI compatible haptic interface to investigate the neural control of arm movements," in *IEEE Int. Conf. Robot. Autom. (ICRA)*, 2006, pp. 3825–3831.

[11] S. Menon *et al.*, "Haptic fMRI: Combining functional neuroimaging with haptics for studying the brain's motor control representation," in *Int. Conf. IEEE Eng. Med. Biol. Soc. (EMBC)*, 2013, pp. 4137–4142.

[12] M. A. Ergin *et al.*, "Design of a new MR-compatible haptic interface with six actuated degrees of freedom," in *IEEE RAS & EMBS Int. Conf. Biomed. Robot. and Biomech. (BioRob)*, 2014, pp. 293–300.

[13] F. Sergi, A. Erwin, and M. K. O'Malley, "Interaction control capabilities of an MR-compatible compliant actuator for wrist sensorimotor protocols during fMRI," *IEEE/ASME Trans. Mechatronics*, 2015. doi: 10.1109/TMECH.2015.2389222.

[14] R. M. Birn, R. W. Cox, and P. A. Bandettini, "Experimental designs and processing strategies for fmri studies involving overt verbal responses," *Neuroimage*, vol. 23, no. 3, pp. 1046–1058, 2004.

[15] J. F. Veneman *et al.*, "Design and evaluation of the LOPES exoskeleton robot for interactive gait rehabilitation," *IEEE Trans. Neural Syst. Rehab. Eng.*, vol. 15, no. 3, pp. 379–386, 2007.

[16] A. Gupta *et al.*, "Design, control and performance of RiceWrist: A force feedback wrist exoskeleton for rehabilitation and training," *Int. J. Robot. Res.*, vol. 27, no. 2, pp. 233–251, 2008.

[17] K.-M. Lee and D. K. Shah, "Kinematic analysis of a three-degrees-of-freedom in-parallel actuated manipulator," *IEEE J. Robot. Autom.*, vol. 4, no. 3, pp. 354–360, 1988.

[18] F. H. Ghorbel *et al.*, "Modeling and set point control of closed-chain mechanisms: Theory and experiment," *IEEE Trans. Contr. Syst. Technol.*, vol. 8, no. 5, pp. 801–815, 2000.

[19] F. H. Ghorbel, R. Gunawardana, and J. B. Dabney, "Experimental validation of a reduced model based tracking control of parallel robots," in *IEEE Int. Conf. Contr. Appl. (CCA)*, 2001, pp. 375–382.

[20] L. Friedman and G. H. Glover, "Report on a multicenter fMRI quality assurance protocol," *J. Magn. Reson. Imag.*, vol. 23, no. 6, pp. 827–839, 2006.

[21] N. Yu *et al.*, "fMRI assessment of upper extremity related brain activation with an MRI-compatible manipulandum," *Int. J. Comput. Assisted Radiology and Surgery*, vol. 6, no. 3, pp. 447–455, 2011.

[22] C. Hollnagel *et al.*, "Brain activity during stepping: A novel MRI-compatible device," *J. of Neurosci. Methods*, vol. 201, no. 1, pp. 124–130, 2011.